Rock Mech Rock Eng (2016) 49:4711–4729
DOI 10.1007/s00603-016-1081-2

ORIGINAL PAPER

Three-Dimensional Numerical Simulation on Triaxial Failure Mechanical Behavior of Rock-Like Specimen Containing Two Unparallel Fissures

Yan-Hua Huang[1] · Sheng-Qi Yang[1] · Jian Zhao[2]

Received: 17 May 2016 / Accepted: 30 August 2016 / Published online: 15 September 2016

Abstract A three-dimensional particle flow code (PFC3D) was used for a systematic numerical simulation of the strength failure and cracking behavior of rock-like material specimens containing two unparallel fissures under conventional triaxial compression. The micro-parameters of the parallel bond model were first calibrated using the laboratory results of intact specimens and then validated from the experimental results of pre-fissured specimens under triaxial compression. Numerically simulated stress–strain curves, strength and deformation parameters and macro-failure modes of pre-fissured specimens were all in good agreement with the experimental results. The relationship between stress and the micro-crack numbers was summarized. Crack initiation, propagation and coalescence process of pre-fissured specimens were analyzed in detail. Finally, horizontal and vertical cross sections of numerical specimens were derived from PFC3D. A detailed analysis to reveal the internal damage behavior of rock under triaxial compression was carried out. The experimental and simulated results are expected to improve the understanding of the strength failure and cracking behavior of fractured rock under triaxial compression.

Keywords Rock mechanics · Triaxial compression · Crack evolution · Internal damage · PFC3D

✉ Sheng-Qi Yang
yangsqi@hotmail.com

[1] State Key Laboratory for Geomechanics and Deep Underground Engineering, School of Mechanics and Civil Engineering, China University of Mining and Technology, Xuzhou 221116, People's Republic of China

[2] Deep Earth Energy Research Laboratory, Department of Civil Engineering, Monash University, Melbourne, VIC 3800, Australia

1 Introduction

Rock is a complex geological medium with many flaws (e.g., joints, fissures, weak surfaces, faults), which are of importance for mining, oil exploration, CO_2 sequestration and nuclear waste storage engineering. Previous studies showed that preexisting flaws have a significant influence on the strength and deformation of rock (Goodman 1989; Palmstrom 1995). Failure in a rock can often take place along pre-flaws. Thus, flaws affect engineering safety and stability. Therefore, studies of the influence of preexisting flaws on the strength failure and cracking behavior of rock are of significance for predicting unstable failure in rock engineering.

Mechanical parameters and crack evolution mechanisms of rock containing preexisting fissures under uniaxial compression have been extensively investigated, such as the effect of the fissure density, fissure length, fissure angle, ligament length and ligament angle (Bobet 2000; Zhu et al. 2016; Fujii and Ishijima 2004; Morgan et al. 2013; Wong and Chau 1998; Yin et al. 2014). However, rock materials are always under three-dimensional stress in real engineering. Hence, it is more important to investigate the influence of preexisting fissures on the strength and failure behavior of rock under triaxial compression. Yang et al. (2008) carried out conventional triaxial compressive tests for marble specimens with two closed fissures in non-overlapping geometry. The experimental results showed that the strength of pre-fissured marble is in better agreement with the nonlinear Hoek–Brown criterion than with the linear Mohr–Coulomb criterion and that the failure modes are dependent on both fissure geometry and confining pressure. Liu et al. (2014) tested rock-like material specimens containing three coplanar fissures by using a true triaxial loading device. They concluded from the test

results that new cracking is initiated with a large angle from preexisting fissures under low confining pressure, while new cracks tend to be parallel to pre-fissures under high confining stress. Huang et al. (2016a) used numerical software named AUTODYN to simulate triaxial compression for sandstone with two preexisting fissures. Based on the simulation results, they found that cracks generally initiated at the inner tips with a small inclination angle.

Preexisting fissures are generally three-dimensional (3D) in nature (Yang et al. 2008), and thus, two-dimensional (2D) cracks do not really reflect the 3D situation. In laboratory test, a 2D fissure is always cut as a through crack in plate specimen; while a 3D fissure is always cut as a surface or internal crack in specimen. For 2D situation, the main cracking patterns are wing crack, anti-wing crack, shear crack, far-field crack and surface spalling (Bobet 2000; Morgan et al. 2013; Wong and Chau 1998; Yin et al. 2014), while for 3D case, the cracking patterns are distinctly different, which results from that cracks may propagate toward the depth and height direction. According to their experiments (Liu et al. 2008; Wong et al. 2004; Yin et al. 2014), wing crack, anti-wing crack, secondary crack, petal crack and shell-like crack can initiate from fissure tips. Cracks occur on 3D faces, leading the evolution mechanism much more complicated. Dyskin et al. (1994, 1999) reported that the major difference between 2D and 3D crack propagation mechanisms is the maximum possible size of 3D wing cracks and developed a 3D model to analyze the reason why the experimentally observed crack growth was only moderate. Based on the classical fracture mechanics theory, Lu et al. (2015) discussed the failure mechanism of 3D surface crack. However, due to the complex stress state around a 3D crack, it is very difficult to understand the fracture mechanism and establish a quantitative model to accommodate the 3D cracking process (Liang et al. 2012; Lu et al. 2015). Therefore, laboratory experiment and numerical simulation are effective methods to investigate the 3D fracture behavior. Equipment (e.g., acoustic emission), special materials (e.g., transparent material) and numerical software (e.g., RFPA3D) are needed to study 3D crack evolution behavior. Sahouryeh et al. (2002) and Dyskin et al. (2003) conducted a series of uniaxial and biaxial compression tests for transparent resin specimens with a single fissure. Their test results indicated that 3D crack evolution differs from 2D behavior. Liu et al. (2008) investigated the crack growth process of surface faults under biaxial compression using a multi-channel digital strain gauge (MCDSG), digital speckle correlation method (DSCM) and acoustic emission (AE) location system. Liang et al. (2012) simulated the fracture characteristics of rock specimens containing a preexisting surface flaw using RFPA3D. Wing cracks, anti-wing cracks and shell-like cracks were reproduced in their study, and the mechanism of 3D crack propagation was discussed. Yang et al. (2014a) performed several laboratory tests and FRANC3D numerical simulations for rock-like material specimens with internal fissures to study the strength and failure behavior under uniaxial tension. Wang et al. (2014) verified the experimental results on pre-fissured marble under triaxial compression, which were carried out by Yang et al. (2008), and then analyzed the influences of rock heterogeneity and fissure geometry on the strength and 3D propagation processes of two closed fissures.

The particle flow code named PFC, which is a discrete element method (DEM), has been widely applied in uniaxial compressive test modeling (Cao et al. 2016; Lee and Jeon 2011; Yang et al. 2014b) and biaxial compressive test modeling (Huang et al. 2016d; Manouchehrian et al. 2014). PFC2D was used for rock containing preexisting fissures, and PFC3D was applied for intact or joint rock (Bahaaddini et al. 2013; Ding et al. 2014; Fan et al. 2015; Turichshev and Hadjigeorgiou 2015; Zhou et al. 2014). Recently, unparallel fissures have received much attention. Preliminary experimental and numerical results regarding unparallel fissures were reported by Haeri et al. (2014), Lee and Jeon (2011) and Yang et al. (2014b). However, most of those results were limited to 2D crack propagation. In addition, there have been few reports in the literature regarding crack evolution experiments of unparallel fissures under triaxial compression. Therefore, a systematic laboratory triaxial compressive test was carried out in our study for cylindrical rock-like material specimens containing two unparallel fissures to better understand the fracture-mechanical behavior of fractured rock. Moreover, PFC3D was applied to investigate 3D crack initiation, propagation and the coalescence process of preexisting fissures. Finally, horizontal and vertical cross sections of numerical specimens after failure were obtained to explore the internal damage behavior under triaxial compression.

2 Numerical Model and Micro-Parameters

2.1 Brief Description of Laboratory Test

Cement, sand and water (1:0.8:0.35) were used to fabricate rock-like material. Microstructure surface images of tested rock-like material are shown in Fig. 1. Figure 1 reveals that the geometric shapes of sand are irregular lumps and that cement binds the grains together. The average dry density of the tested rock-like material is approximately 2120 kg/m^3. The basic mechanical parameters (average values) of the tested intact rock-like material specimens can be described as follows. The uniaxial compressive strength was 63.19 MPa, the elastic modulus was 16.98

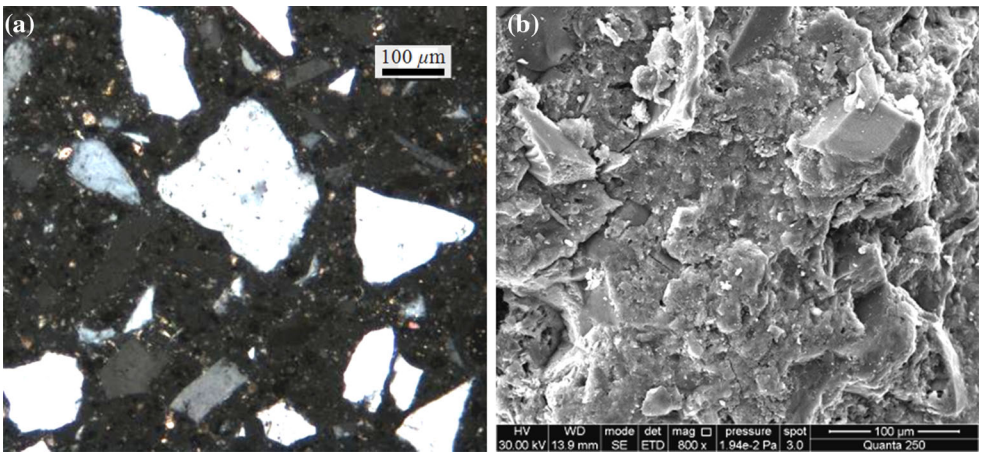

Fig. 1 Microscopic structure of rock-like material. **a** Thin section; **b** scanning electron microscopy (SEM) image

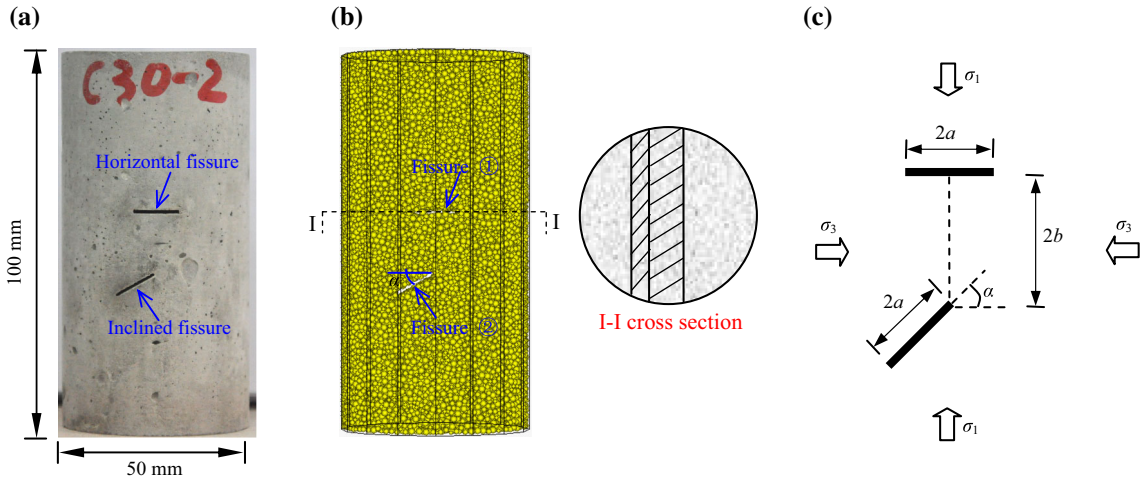

Fig. 2 Specimen containing two unparallel fissures. **a** Laboratory rock-like material specimen; **b** PFC3D model and fissure surface; and **c** fissure geometry and loading condition

GPa, the Poisson ratio was 0.181, the Brazilian tension strength was 6.31 MPa and the cohesion and internal friction angle were 22.83 MPa and 20.50°, respectively. This indicates that the mechanical behavior of fabricated rock-like material in this study agrees well with the general behavior of real rock material, for example brittle sandstone.

All experiments were carried out on cylindrical specimens that had a 50 mm diameter and 100 mm height. To investigate the influences of preexisting fissures on the strength and failure behavior, two unparallel penetrating fissures (horizontal and inclined) were created in the cylindrical specimen as shown in Fig. 2a. The preexisting fissures indicate the artificially created flaws, which were machined by inserting steel into the steel model before pouring the model materials and pulling them out before the completed solidification. The pre-existent fissures would not be filled, which means they were open. The MTS815 rock mechanics servo-controlled testing system was used to conduct uniaxial and conventional triaxial compression tests for intact and pre-fissured rock-like material specimens.

2.2 PFC3D Model Construction

There are two kinds of basic bond models, i.e., contact bond model (CBM) and parallel bond model (PBM) in PFC3D 4.0 version (Itasca Consulting Group Inc. 2008). Parallel bonds can transmit both forces and moments between particles, while contact bonds can only transmit forces acting at the contact point. Moreover, in the PBM, bond breakage can lead to an immediate decrease in macro-stiffness because the stiffness is contributed by both contact stiffness and bond stiffness. Therefore, PBM was

selected for numerical simulations in this study because the PBM is more realistic for rock-like material modeling (Cho et al. 2007; Lee and Jeon 2011; Yang et al. 2015a, b).

In accordance with laboratory tests, a cylindrical model with a size of Φ50 mm × 100 mm was constructed using the same scale as for the experimental specimen. The uniform distribution of balls is more commonly used by researchers, such as Ding et al. (2014), Yang et al. (2014b, 2015b), Zhang et al. (2011). Their simulated results show that the uniform distribution can better modeling the mechanical behavior of rock. The ball radius followed a uniform distribution ranging from 0.7 to 1.12 mm. The particles are spherical balls without considering the particle shape and angularity. We cannot match the physical particle size and shape due to the limitation of computing power in present study. To develop a finer model, a huge number of balls would be needed, which is not suitable for the current cracking analysis. Each numerical intact model was divided into 56,124 balls. Two open fissures were created by ball deletion based on the intact numerical specimen. The geometry of the two fissures is the same as that in laboratory tests, that is, the fissure length 2a = 12 mm, ligament length 2b = 16 mm and fissure angles are 30°, 45° and 60°, respectively. The numerical specimen constructed in the parallel bond model of PFC3D and the fissure geometry are shown in Fig. 2.

2.3 Confirmation for Micro-Parameters

The parallel bond model includes a series of micro-mechanical parameters, such as the Young's modulus of the particle and parallel bond, as well as the normal and shear stiffness of the particle and parallel bond, which determine the macro-mechanical response of the numerical specimen. Appropriate values for these micro-mechanical parameters should be selected before modeling through a calibration process. In this research, the micro-parameters were confirmed by using the trial and error method. The macroscopic behavior of intact rock-like material specimen obtained by experiment was used to calibrate the micro-parameters. The macroscopic results obtained by numerical simulation after each trial was used to check the micro-parameters. This process was repeated until the numerical results of intact rock-like material specimen achieved a good agreement with the experimental results. After numerous calibrations, we derived the micro-mechanical parameters for rock-like material (Table 1), which can be described in detail as follows. The Young's modulus of the ball and parallel bond both are 12.3 GPa, and the ratios of the normal to shear stiffness of the ball and parallel bond both are 1.4. The ball friction coefficient is 0.35. The mean values of parallel bond normal and shear strength are 43 and 60 MPa, respectively. The standard deviations of parallel bond normal and shear strength are 6 and 9 MPa, respectively.

Figure 3 shows the comparison between experimental and numerical results of intact rock-like material specimen under uniaxial and triaxial compression. It can be seen that the numerical curve under uniaxial loading agrees well with the experimental curve (Huang et al. 2016c), including the elastic deformation stage, peak stress and brittle drop at post-peak stage. Moreover, the shape of the numerically simulated stress–strain curve under triaxial compression is also in excellent agreement with the experimental results, besides the stage of residual strength.

Figure 3b shows clearly that the simulated triaxial compressive strength is similarly equal to that obtained in the experiment under the same confining pressure (Huang et al. 2016b). The dispersion extent is defined as the percentage ratio of the absolute difference between the experimental and numerical value and average value. The dispersion extent is approximately 5.5 % for $\sigma_3 = 5$ MPa, whereas it is smaller for other confining pressures (<2.0 %). Moreover, we can see that the triaxial compressive strength of intact rock-like material increases linearly with increasing confining pressure, which can be expressed by the linear Mohr–Coulomb criterion. In accordance with the linear Mohr–Coulomb criterion, the values of the cohesion internal friction angle of the numerical model are 22.88 MPa and 19.97°, respectively, implying that the strength parameters are approximately equal to those obtained by experiment.

3 Numerically Simulated Results of Pre-fissured Specimens

Micro-mechanical parameters for the intact numerical rock-like material were obtained through calibration and verification processes. There is no need to calibrate the micro-mechanical parameters for the pre-fissured numerical specimen again, which means that for the simulation of the pre-fissured numerical specimen, the same values are used as for the intact specimen (Lee and Jeon 2011; Yang et al. 2014b). A systematic simulation for pre-fissured specimens and a comparison with the experimental results were made to better understand the strength and failure behavior of rock containing two unparallel fissures under triaxial compression. Axial deviatoric stress–strain curves, strength and deformation parameters and macro-failure modes are presented in this section, and the numerical results are quantitatively compared with the experimental results.

3.1 Stress–Strain Behavior

Axial deviatoric stress–axial strain and circumferential strain curves of rock-like material specimens from PFC3D simulation and experiments under conventional triaxial compression are presented in Fig. 4.

Table 1 Micro-mechanical parameters for rock-like material in PFC3D

Micro-parameters	Values	Remarks
Minimum radius of the ball, R_{min} (mm)	0.70	Parameter of ball
Ratio of maximum to minimum of radius, R_{rat}	1.60	Parameter of ball
Density of the ball, ρ (kg/m^3)	2120	Parameter of ball
Friction coefficient, μ	0.35	Parameter of ball
Young's modulus of the ball, E_c (GPa)	12.3	Parameter of ball
Ratio of normal to shear stiffness of the ball, k_n/k_s	1.40	Parameter of ball
Young's modulus of the parallel bond, $\bar{E}_c$ (GPa)	12.3	Parameter of parallel bond
Ratio of normal to shear stiffness of the parallel bond, $\bar{k}_n/\bar{k}_s$	1.40	Parameter of parallel bond
Parallel bond normal strength (σ_n), mean (MPa)	43.0	Parameter of parallel bond
Parallel bond normal strength, standard deviation (MPa)	6.0	Parameter of parallel bond
Parallel bond shear strength (τ_n), mean (MPa)	60.0	Parameter of parallel bond
Parallel bond shear strength, standard deviation (MPa)	9.0	Parameter of parallel bond

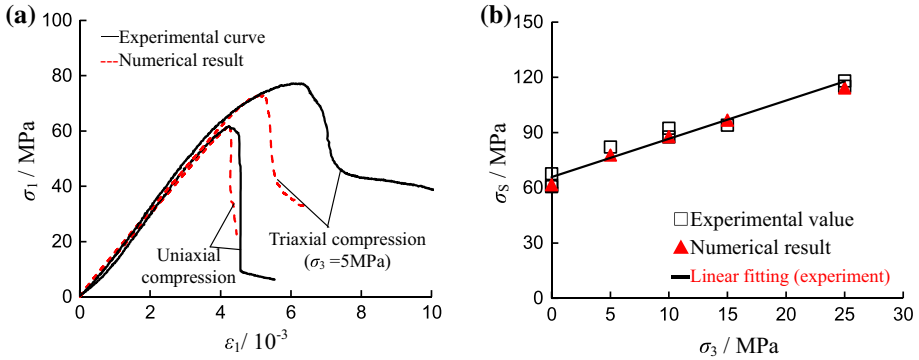

Fig. 3 Comparison between numerical and experimental results of intact specimens. **a** Axial stress–strain curve; and **b** peak strength

The experimental curves under uniaxial and triaxial compression were obtained from Huang et al. (2016b, c). Black solid lines in Fig. 4 represent experimental curves, and numerical curves are shown as red dotted lines. Figure 4 shows that the PFC3D numerically simulated stress–strain curves all are in good agreement with the experimental results except for $\alpha = 30°$ under confining pressures of 5 and 15 MPa. The slope rate in the linear elastic stage, peak stress and brittle response in the post-peak stage obtained from experimental and numerical curves of pre-fissured specimens are similar for $\alpha = 30°$, 45° and 60° under uniaxial compression. Under triaxial compression, the elastic stage of numerical curves agrees well with the experimental curves for $\alpha = 30°$, 45° and 60°. Moreover, the numerical curves are similar to the experimental curves after peak stress, i.e., both the numerical and experimental curves reach the residual strength. However, some experimental curves show lower residual strength, such as $\alpha = 30°$, under confining pressures of 5, 15 and 25 MPa, which may be affected by the hydraulic oil in the laboratory tests.

3.2 Strength and Deformation Properties

The stress–strain behavior from PFC3D modeling was qualitatively compared with the experimental results. In the following section, the numerical peak strength and peak strain are quantitatively compared with the experimental values.

Figure 5 shows a comparison between the numerical strength and deformation parameters, e.g., peak strength and peak strain, and experimental values under different confining pressures for pre-fissured specimens. It can be seen that numerically simulated triaxial compressive strengths are approximatively equal to the experimental values for both $\alpha = 45°$ and 60°, except for $\alpha = 30°$ (Fig. 5a–c). However, the strength simulated by PFC3D has a similar trend with confining pressure. Both the numerical and experimental strength increase with the confining pressure. In addition, the increase rate from 0 to 5 MPa is higher than that in the range of 5–25 MPa. For $\alpha = 30°$, the dispersion extent is approximately 22.8 % for uniaxial compression and approximately 15.1 % for $\sigma_3 = 5$, 10 and 25 MPa. The dispersion extent is much smaller for $\sigma_3 = 25$ MPa, which equals 7.2 %. For $\alpha = 45°$, the dispersion extent is approximately 13.0 % for $\sigma_3 = 5$ and 10 MPa, while the extent is approximately 4.3 % for uniaxial compression and $\sigma_3 = 15$ and 25 MPa. Furthermore, for $\alpha = 60°$, the dispersion extents are approximately 3.3, 3.4, 6.5, 1.9 and 4.9 % for

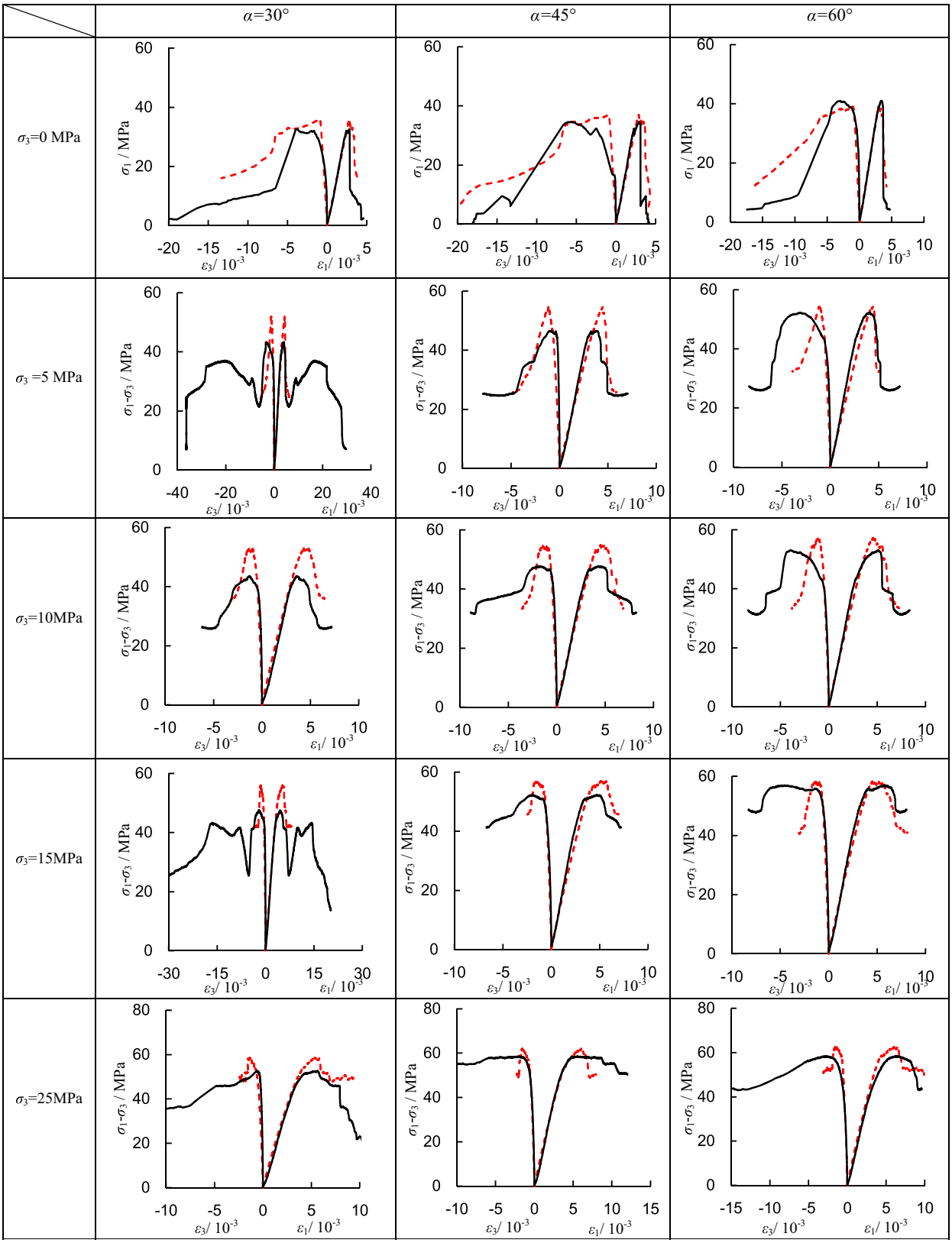

Fig. 4 Stress–strain curves of fissured specimens obtained through experiment and simulation. *Black solid lines* in this figure represent experimental curves, and numerical curves are shown as *red dotted lines* (color figure online)

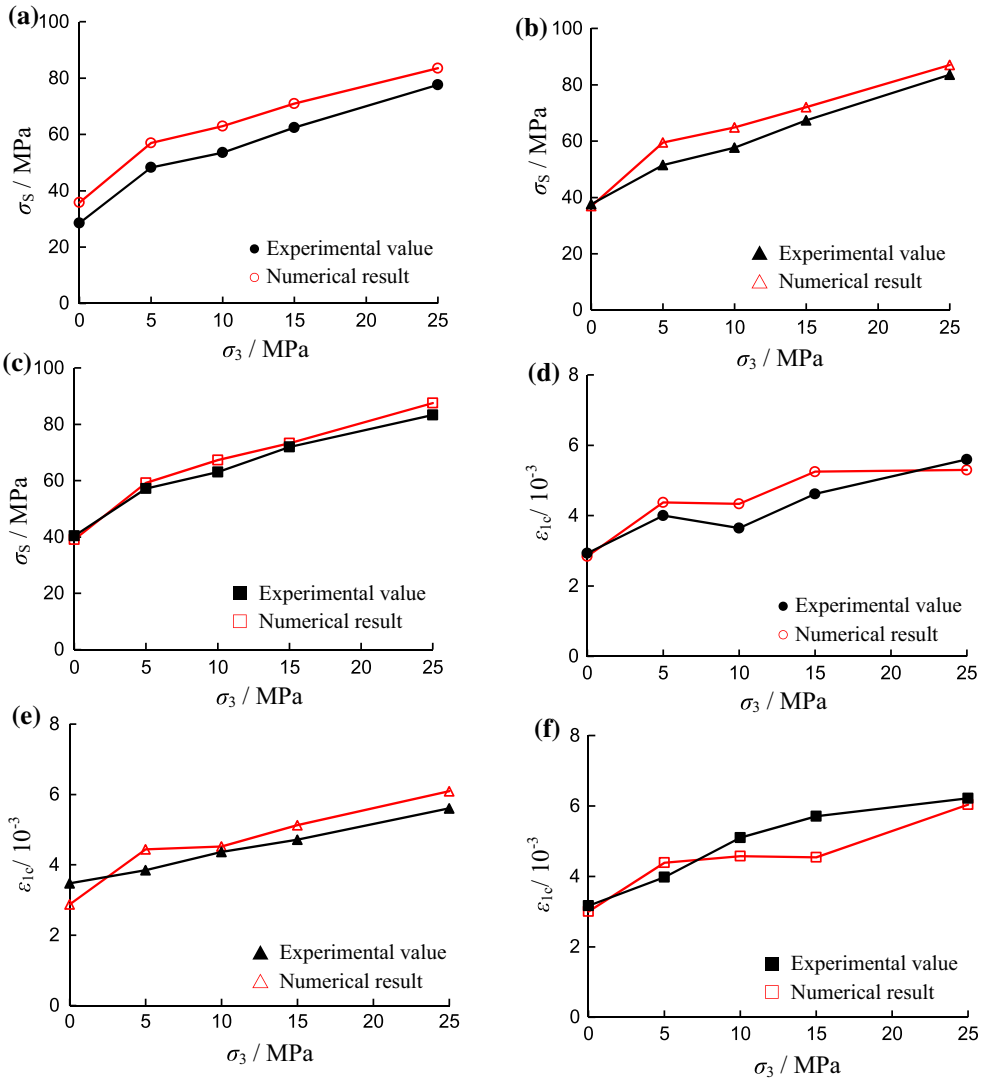

Fig. 5 Comparison between numerical and experimental peak strength and peak strain of pre-fissured specimens. **a** $\alpha = 30°$, peak strength; **b** $\alpha = 45°$, peak strength; **c** $\alpha = 60°$, peak strength; **d** $\alpha = 30°$, peak strain; **e** $\alpha = 45°$, peak strain; and **f** $\alpha = 60°$, peak strain

$\sigma_3 = 0$–25 MPa, which are smaller than those for $\alpha = 30°$ and 45°.

The numerical axial peak strains all agree well with the experimental values (Fig. 5d–f) for both the value of peak strain and the trend with the confining pressure. The axial peak strains all increase with the confining pressure. The difference between numerical and experimental axial peak strain can be explained as follows. For $\alpha = 30°$, the dispersion extent is approximately 3.1 % for uniaxial compression and 17.2 % for $\sigma_3 = 10$ MPa, whereas the dispersion extent is in the range of 9.1 % for $\sigma_3 = 5$, 15 and 25 MPa. For $\alpha = 45°$, the extent is approximately 16.6 % for uniaxial compression and $\sigma_3 = 5$ MPa and 8.3 % for $\sigma_3 = 15$ and 25 MPa, whereas the extent is much smaller for $\sigma_3 = 10$ MPa, which approximately equals to 3.5 %. For $\alpha = 60°$, the maximum dispersion extent is approximately 22.7 % for $\sigma_3 = 15$ MPa and the minimum dispersion extent is approximately 2.9 % for $\sigma_3 = 25$ MPa, while for uniaxial compression and $\sigma_3 = 5$ and 10 MPa, the dispersion extents are 5.4, 9.9 and 10.9 %, respectively.

3.3 Macro-Failure Modes

Figure 6 further depicts the influences of the confining pressure and fissure angle on the ultimate failure modes of rock-like material specimens containing two unparallel fissures under uniaxial and triaxial compression by PFC3D numerical simulation. Ultimate experimental failure modes are given for comparison in Fig. 6.

In Fig. 6, the experimental failure modes under uniaxial and triaxial compression were taken from Huang et al. (2016b, c). When the bond between adjacent parent balls is broken in the PBM, a micro-crack forms. A micro-crack is represented as a segment. The tensile micro-crack is shown

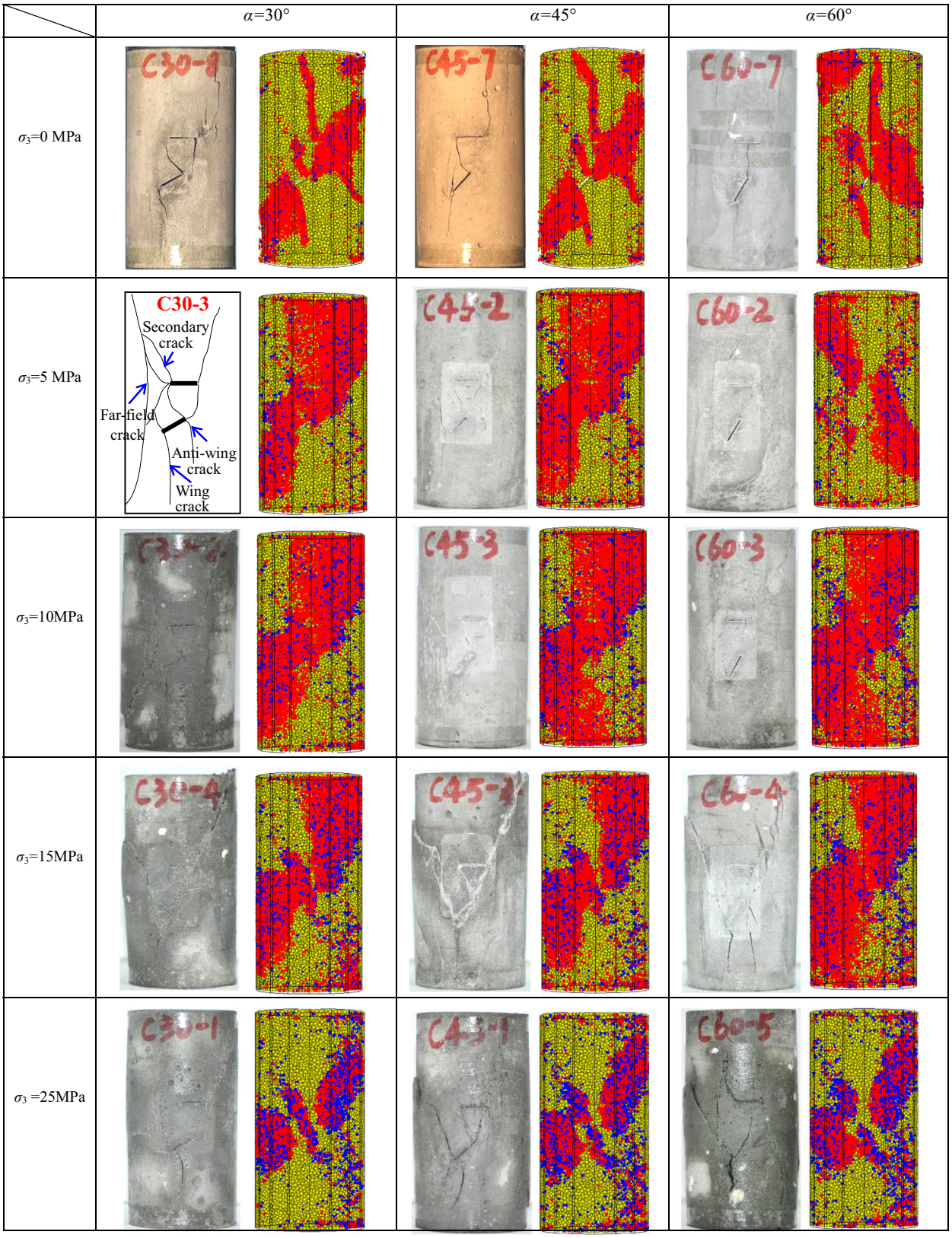

Fig. 6 Failure modes of fissured specimens obtained through experiment and simulation. The *left figure* shows the experimental failure mode, and the *right figure* presents the numerical failure mode in each rigid

as a red line, and the shear crack is shown as a blue line in the numerical results. In this paper, a macro-crack was defined when enough micro-cracks were connected.

As shown in Fig. 6, we can conclude that the ultimate numerical failure modes of rock-like material containing two unparallel fissures simulated by PFC3D are similar to those obtained from laboratory experiments. Moreover, Fig. 6 shows that the failure modes of pre-fissured specimens are determined by the confining pressure and fissure angle. The basic principle can be described as follows. When the confining pressure is small, it is mainly affected by the fissure angle, whereas it is mainly affected by the confining pressure when the confining pressure is high.

The systematic comparison, including the stress–strain curves, strength and deformation parameters and failure modes of rock-like material specimens containing two unparallel fissures under uniaxial and triaxial compression are shown in Figs. 4, 5 and 6, respectively, indicates that the calibrated numerical mode reproduces the strength failure behavior of laboratory physical experiments and proves the reasonability and accuracy of the micro-mechanical parameters used in PFC3D given in Table 1.

4 Cracking Behavior of Pre-fissured Specimens

4.1 Micro-crack Number Evolution

Figure 7 illustrates the relationship between the micro-crack number and axial deviatoric stress of intact and pre-fissured numerical specimen under uniaxial and triaxial compression.

The number of micro-cracks generally increases with deformation, and the increasing rate of micro-crack number evolves during the process of crack initiation, propagation and coalescence (Fig. 7). The evolution characteristics of

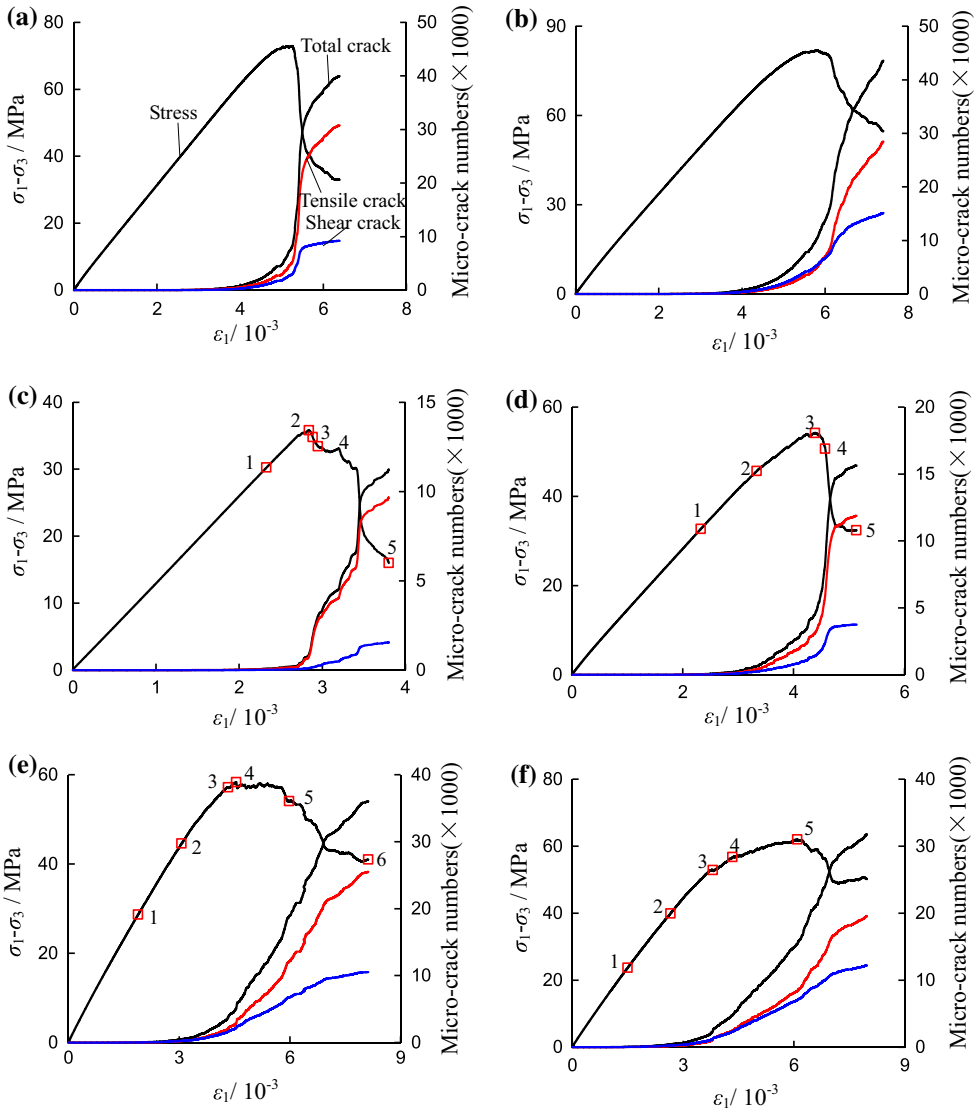

Fig. 7 Relation between axial strain level of the stress–strain curve and the number of micro-cracks. **a** Intact specimen, $\sigma_3 = 5$ MPa; **b** intact specimen, $\sigma_3 = 15$ MPa; **c** pre-fissured specimen ($\alpha = 30°$), $\sigma_3 = 0$ MPa; **d** pre-fissured specimen ($\alpha = 60°$), $\sigma_3 = 5$ MPa; **e** pre-fissured specimen ($\alpha = 60°$), $\sigma_3 = 15$ MPa; and **f** pre-fissured specimen ($\alpha = 45°$), $\sigma_3 = 25$ MPa

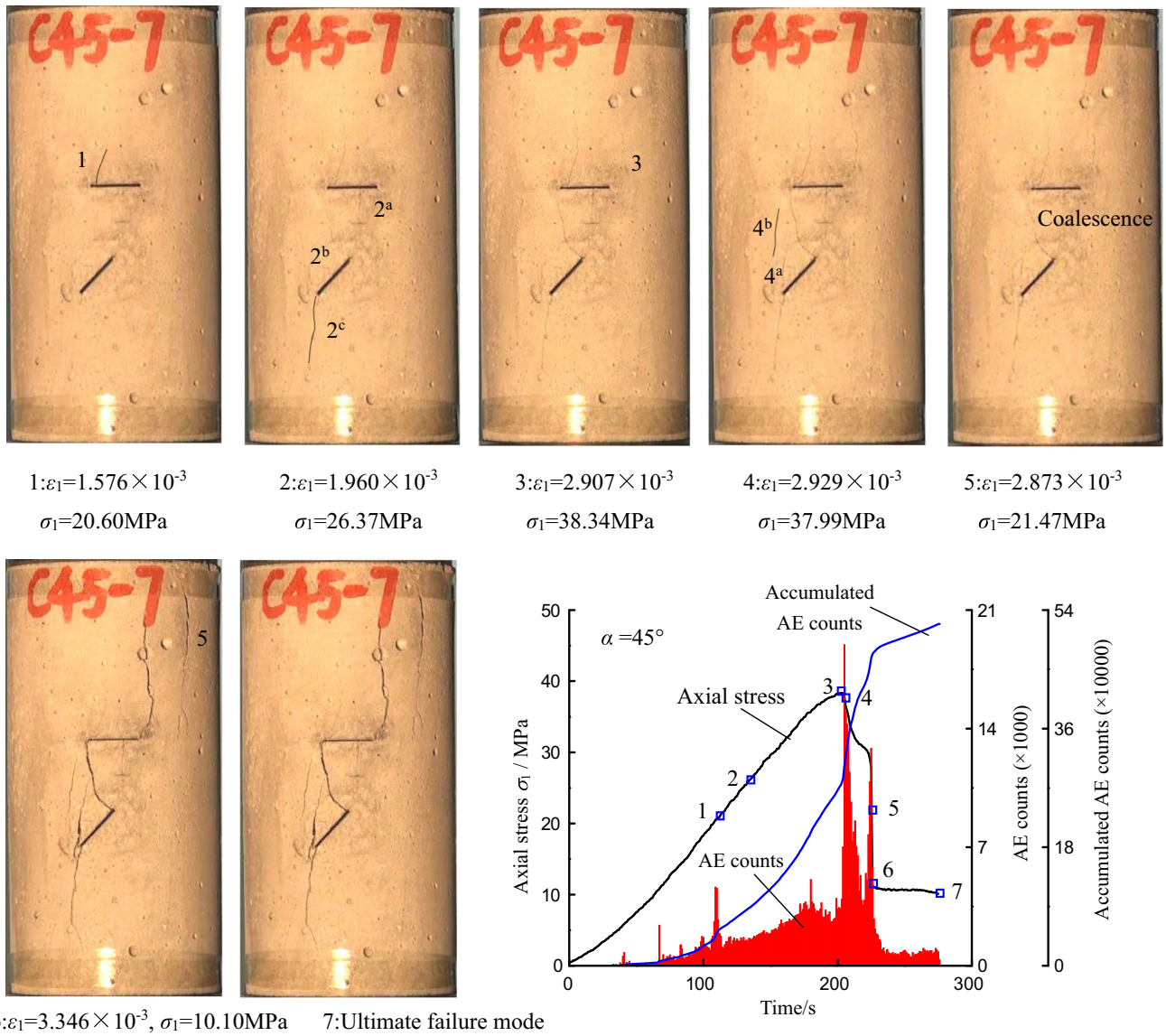

Fig. 8 AE counts and crack evolution process of rock-like material specimen containing two unparallel fissures for $\alpha = 45°$ under uniaxial compression obtained from laboratory experiment

the micro-crack number in linear elastic deformation, nonlinear deformation, post-peak strain softening and the residual strength stages can be summarized as follows. In the stage of linear elastic deformation, a few micro-cracks can be observed in the accumulated micro-crack number curve, but only when the stress increased to some extent. From the stage of linear elastic deformation to nonlinear deformation, more micro-cracks were formed, which can be verified from the slow increase in micro-cracks. We can see that the micro-crack number increases faster than other phases after the stress peaks. However, some micro-cracks still form in the stage of residual strength, and the increase rate in this phase is much smaller than that of former stages.

In addition, the stress–strain curve for intact numerical specimens showed a stronger brittle behavior in the stage of post-peak under low confining pressure (e.g., 5 MPa) than under high confining pressure (e.g., 15 MPa). In contrast, the increasing rate of the micro-crack number curve was larger under low confining pressure than under high confining pressure. A similar situation can also be observed for numerical specimens containing two unparallel fissures. The stronger the brittle response of the stress–strain curve, the faster the increase in micro-crack number curve. Moreover, tensile cracks were dominant during deformation, indicating that the major mode was under tension for numerical specimens.

4.2 Crack Coalescence Process Obtained by Experiment and Modeling

Figure 8 presents the axial stress–time curves, output of AE counts, curve of the accumulated AE counts and crack evolution process of rock-like material specimens containing two unparallel fissures obtained from the laboratory experiment. The Arabic numbers in Fig. 8 denote the order of cracking in the pre-fissured specimen observed by photographic monitoring, and the superscript letters on the same number indicate that these cracks were simultaneously initiated at different positions.

In accordance with Fig. 8, the AE and real-time crack coalescence behavior of rock-like specimen containing two unparallel fissures ($\alpha = 45°$) are analyzed during the entire deformation. At the initial deformation and low stress level stages, no macro-cracks are observed in the specimen surface. However, the obvious AE counts are clearly seen, which may result from the initiation of micro-cracks in the specimen interior. When the axial stress reaches point 1, crack 1 is initiated away from the left tip of the horizontal fissure. After point 1, the axial stress increases linearly as time increases. When the specimen is loaded to point 2 ($\sigma_1 = 26.37$ MPa), crack 2^a is formed away from the right tip of the horizontal fissure, while cracks 2^b and 2^c are initiated at the lower and upper tips of the inclined fissure, respectively. The initiation of crack 1 and crack $2^{a–c}$ does not lead to a stress drop or a large AE event. When the axial stress increases to the peak stress, i.e., point 3, crack 3 emanates near the right tip of the horizontal fissure. After the strength peaked, the corresponding axial stress of the specimen begins to decrease as deformation increases. The occurrence of crack 4^a and crack 4^b in the ligament region leads to a small stress drop to 36.48 MPa when the axial stress decreases to point 4 ($\sigma_1 = 37.99$ MPa). The largest AE event appears at that time. The coalescence of crack 2^b between the left tip of the horizontal fissure and the upper tip of the inclined fissure contributes to a large stress drop from 27.78 to 11.35 MPa, and a large AE event can simultaneously be observed at point 5 ($\sigma_1 = 21.47$ MPa). With the increase in deformation, the axial stress decreases to point 6 ($\sigma_1 = 10.10$ MPa), a far-field crack 5 emanates at the top of the specimen and propagates downwards approximately in parallel with the direction of axial stress. The width of the cracks that are formed before point 5 increases, except for crack 1. Our analysis shows that the corresponding axial stress drop in the axial stress–time curve and a large AE event can simultaneously be observed when a new crack formed or crack coalescence occurred in a pre-fissured specimen.

However, it is difficult to directly observe the crack evolution process due to the closed environment in laboratory physical triaxial compression tests. To better understand the strength and failure behavior, it is essential to establish a correlation between the stress level and fracture order of specimens containing preexisting fissures. In the following section, the cracking process of specimen containing two unparallel fissures obtained by PFC3D modeling is discussed, and the relationship between fracture process and stress level is analyzed. Figure 9 presents the crack coalescence process of numerical specimens containing two unparallel fissures for $\alpha = 30°$ under uniaxial compression (Fig. 9a), $\alpha = 60°$ under a confining pressure of 5 MPa (Fig. 9b), $\alpha = 60°$ under a confining pressure of 15 MPa (Fig. 9c) and $\alpha = 45°$ under a confining pressure of 25 MPa (Fig. 9d). The four crack coalescence processes reveal different crack evolution types, different fissure angles (i.e., 30°, 45° and 60°) and different confining pressures (i.e., 0 MPa, low pressure of 5 MPa, medium pressure of 15 MPa and high pressure of 25 MPa). It should be noted that the numbers in Fig. 9 correspond to the crack order shown in Fig. 7.

In accordance with Figs. 7c and 9a, we can analyze the real-time crack initiation, propagation and coalescence process of rock-like material specimen containing two unparallel fissures for $\alpha = 30°$ under uniaxial compression. When the axial stress reaches 30.25 MPa (point 1 in Fig. 7c), three tensile wing cracks are formed from the two tips of the horizontal fissure and lower tip of the inclined fissure. With the increase in axial deformation after point 1, the pre-fissured specimen is loaded to 35.81 MPa (point 2 in Fig. 7c) and a tensile wing crack is formed at the upper tip of the inclined fissure. An anti-wing crack emerges from the lower tip of the inclined fissure at that moment, and an axial tensile crack is observed at a distance from the right tip of the horizontal fissure. When the specimen is loaded to point 3 ($\sigma_1 = 34.81$ MPa), the original cracks extend. The first crack coalescence between the right tip of the horizontal fissure and the upper tip of the inclined fissure can be seen due to the propagation of tensile wing crack initiated at the right tip of the horizontal fissure. With the continuous increase in axial deformation, the axial stress increases to point 4 ($\sigma_1 = 33.43$ MPa). At this time, the tensile crack initiated at the upper tip of the inclined fissure grows and forms a link to the left tip of the horizontal fissure. Subsequently, far-filed cracks and secondary cracks emanate in the ultimate failure specimen. The crack evolution process obtained by PFC3D agrees well with that of the laboratory specimen (Huang et al. 2016b).

Figure 9b shows that two tensile cracks are initiated at the two tips of the horizontal fissure for $\alpha = 60°$ under a low confining pressure of 5 MPa when the axial deviatoric stress reaches 32.71 MPa (point 1 in Fig. 7d). With increasing axial deformation, cracks continue to propagate and the downward growth is faster than the upward growth. After the

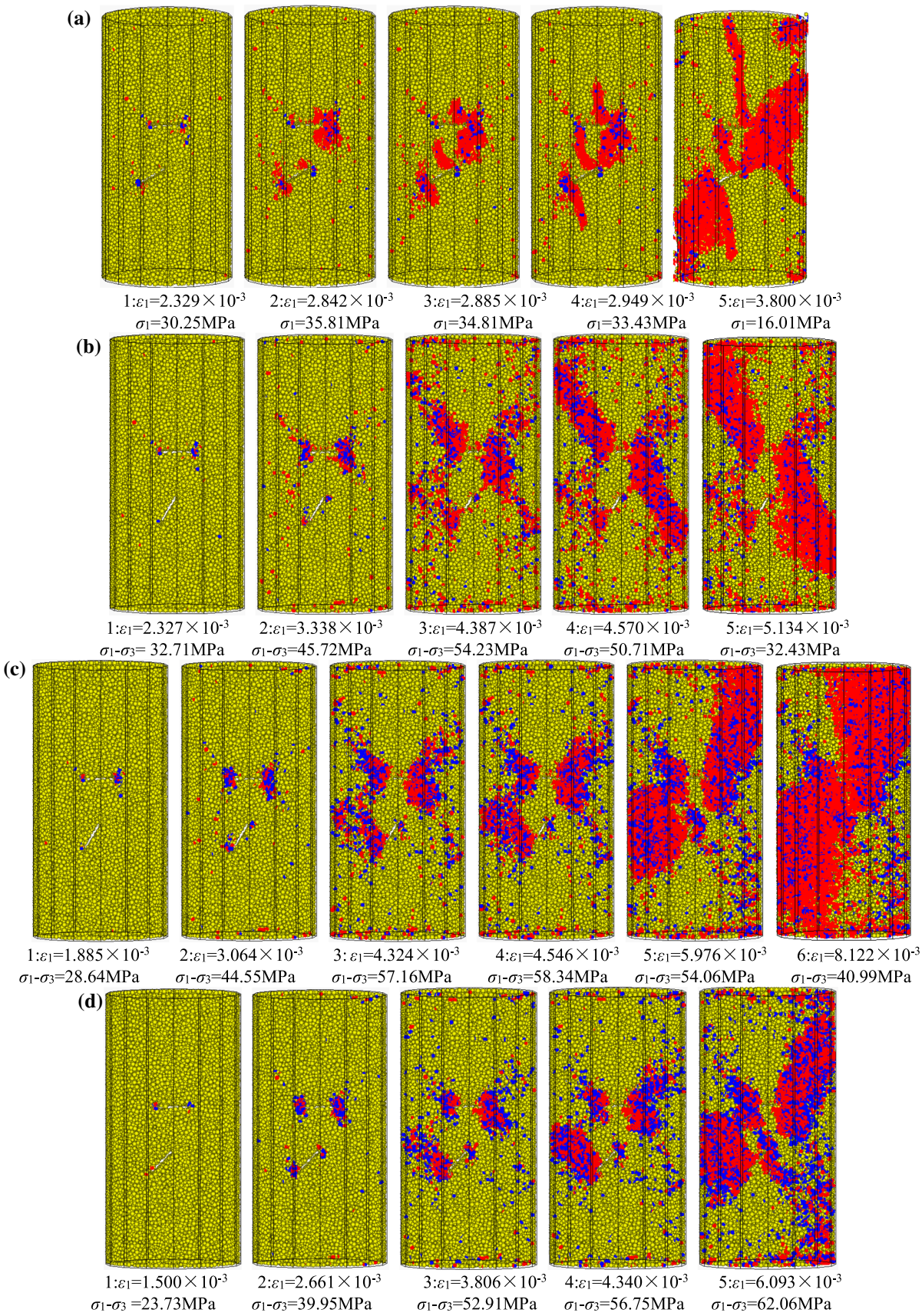
(a)
1:ε_1=2.329×10^{-3} σ_1=30.25MPa
2:ε_1=2.842×10^{-3} σ_1=35.81MPa
3:ε_1=2.885×10^{-3} σ_1=34.81MPa
4:ε_1=2.949×10^{-3} σ_1=33.43MPa
5:ε_1=3.800×10^{-3} σ_1=16.01MPa
(b)
1:ε_1=2.327×10^{-3} σ_1-σ_3= 32.71MPa
2:ε_1=3.338×10^{-3} σ_1-σ_3=45.72MPa
3:ε_1=4.387×10^{-3} σ_1-σ_3=54.23MPa
4:ε_1=4.570×10^{-3} σ_1-σ_3=50.71MPa
5:ε_1=5.134×10^{-3} σ_1-σ_3=32.43MPa
(c)
1:ε_1=1.885×10^{-3} σ_1-σ_3=28.64MPa
2:ε_1=3.064×10^{-3} σ_1-σ_3=44.55MPa
3: ε_1=4.324×10^{-3} σ_1-σ_3=57.16MPa
4:ε_1=4.546×10^{-3} σ_1-σ_3=58.34MPa
5:ε_1=5.976×10^{-3} σ_1-σ_3=54.06MPa
6:ε_1=8.122×10^{-3} σ_1-σ_3=40.99MPa
(d)
1:ε_1=1.500×10^{-3} σ_1-σ_3 =23.73MPa
2:ε_1=2.661×10^{-3} σ_1-σ_3=39.95MPa
3:ε_1=3.806×10^{-3} σ_1-σ_3=52.91MPa
4:ε_1=4.340×10^{-3} σ_1-σ_3=56.75MPa
5:ε_1=6.093×10^{-3} σ_1-σ_3=62.06MPa

◀**Fig. 9** Crack coalescence process of pre-fissured rock-like material specimens under triaxial compression. **a** Pre-fissured specimen ($\alpha = 30°$), $\sigma_3 = 0$ MPa; **b** pre-fissured specimen ($\alpha = 60°$), $\sigma_3 = 5$ MPa; **c** pre-fissured specimen ($\alpha = 60°$), $\sigma_3 = 15$ MPa; and **d** pre-fissured specimen ($\alpha = 45°$), $\sigma_3 = 25$ MPa

tensile cracks grow to a certain length, cracks begin to emerge at the tips of the inclined fissure as shown in point 2 of Fig. 9b. The continuous increase in axial deformation leads to the specimen being loaded to peak strength (point 3 in Fig. 7d). At that time, all cracks in the specimen propagate notably. In particular, the tensile wing crack initiated at the right tip of the horizontal fissure almost forms a link to the upper tip of the inclined fissure. Subsequently, no new cracks generate with the continuous increase in axial deformation, but existing cracks gradually propagate. No crack coalescence can be observed in the failed specimen between the two preexisting fissures. This phenomenon is in good agreement with the laboratory results (Fig. 6).

The cracking behavior of rock-like material specimens containing two unparallel fissures is distinctly different from that under uniaxial compression and low confining pressure (e.g., 5 MPa) when the confining pressure increases to medium (e.g., 15 MPa) and high pressure (e.g., 25 MPa). Several crack coalescences between the two preexisting fissures can be observed in the failed specimens (Fig. 9c, d). The crack coalescence between two unparallel fissures appears first in the specimen, which is due to the link between tensile wing crack forming at the left tip of the horizontal fissure and anti-wing crack at the lower tip of the inclined fissure. Further increase in axial deformation leads to the second crack coalescence between the left tip of the horizontal fissure and the upper tip of the inclined fissure due to the connection of two tensile wing cracks, which is different from the crack coalescence type under uniaxial compression (Fig. 9a). The third crack coalescence occurs between the right tip of the horizontal fissure and the upper tip of the inclined fissure because of the propagation of the wing crack from the right tip and the original tensile wing crack from upper tip.

Furthermore, it can be seen from Fig. 9 that the crack initiation, propagation and the coalescence process depend on the fissure angle and confining pressure. In accordance with Figs. 6 and 9, some significant characteristics can be summarized as follows.

1. The cracking modes are closely related to the fissure angle and confining pressure. Under uniaxial compression, cracks often initiate at a distance away from the tips of horizontal fissure, whereas cracks always emerge from the tips of inclined fissure. However, under triaxial compression, cracks are easier to generate from the tips of horizontal and inclined fissures. As the confining pressure increases, anti-cracks from the lower tip of inclined fissure become easier to initiate and propagate, while the wing cracks are suppressed.
2. The crack coalescence modes between the two preexisting fissures are dependent to the fissure angle and confining pressure. Under uniaxial compression, crack coalescence occurs between the upper tip of the inclined fissure and the two tips of the horizontal fissure for fissure angle of 30°; while crack coalescence occurs due to the propagation of a crack initiated from the upper tip of the inclined fissure to the middle of the horizontal fissure when fissure angles are 45° and 60°. The crack coalescence modes shift gradually with increasing confining pressure.
3. The failure modes depend on the confining pressure. On the macroscopic view, under uniaxial compression and low confining pressure, tensile cracks are dominant in the specimen, and the specimen fails under tensile mode. However, under high confining pressure, shear cracks are more than tensile cracks and shear failure occurs in the specimen. On the mesoscopic view, with the increase in confining pressure, the contribution of tensile micro-cracks (red color in Figs. 6, 9) to the failure decreases gradually, whereas that of shear micro-cracks (blue color in Figs. 6, 9) increases.

4.3 Internal Damage Behavior

Analysis of the pattern of cracks at different positions will improve understanding of internal damage behavior of rock under triaxial compression because the cracks in cylindrical rock specimens are three-dimensional. The numerical specimen can be illustrated by block structures using the Cluster command in PFC3D. The Itasca Consulting Group Inc. (2008) notes: *all particles in the viewing area are added to the view list, with their color determined by their connection with a cluster. A cluster is defined as a set of balls, all of which can be reached by traversing intact bonds*. After the numerical specimen is displayed as a cluster assembly, horizontal cross sections with different heights and vertical cross sections with different depths can be obtained.

Figure 10 illustrates the cluster assembly and the cross-section directions. Figure 10b shows the cluster assembly, which corresponds with the numerical failed specimen shown in Fig. 10a. The slice images for the horizontal cross section shown in Fig. 10c were captured at 10-mm intervals. Each image was 10 mm thick with an up-to-down scanning sequence. The slice images of

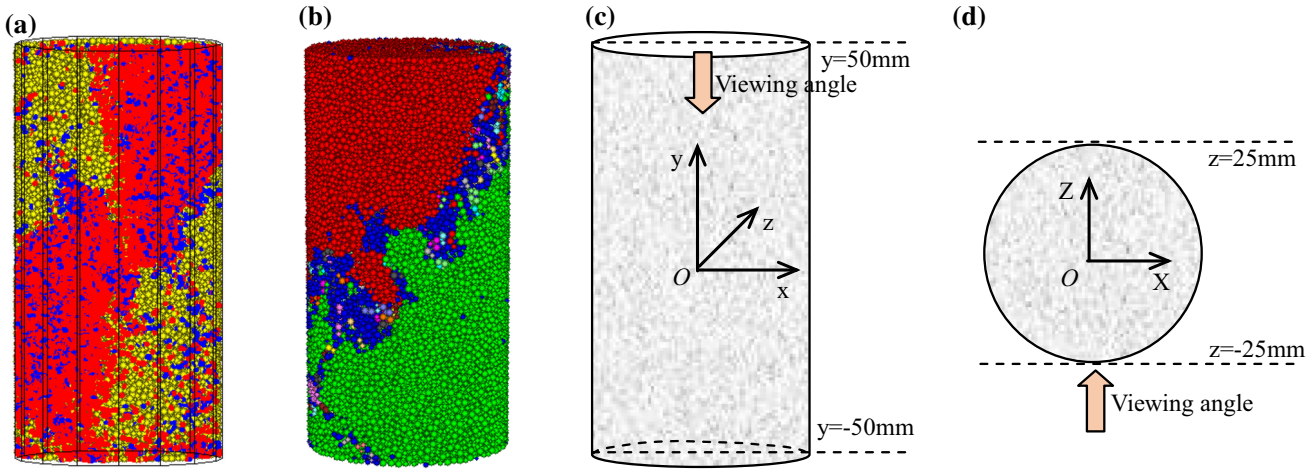

Fig. 10 Illustrations of the cluster assembly and the directions of cross sections. **a** Numerical failed specimen; **b** cluster assembly; **c** viewing angle of horizontal cross section; and **d** viewing angle of front vertical cross section

the front vertical cross section shown in Fig. 10d were captured at 5-mm intervals, and each image was 5 mm thick with a front-to-back scanning sequence. In the cluster assembly and cross-section images, the adjacent balls with same color are a cluster element in the respective image.

Figure 11 presents the cross-section results of the intact numerical specimen after triaxial compression failure, including front vertical cross sections with different depths (Fig. 11a) and horizontal cross sections with different heights (Fig. 11b). The slice image in Fig. 11a at $z = -25$ mm demonstrates the surface crack distribution. Only one main crack is located in the top region of the specimen, and some minor fractures are observed in bottom region. Compared with the actual surface crack photograph (Fig. 11a), it is clear that the numerical surface image approximates the experimental physical specimen. The fracture in the top region of the specimen continuously propagates from $z = -20$ mm to -5 mm, and with increasing depth, the under fracture also gradually grows. The slice image demonstrates the central crack distribution at $z = 0$ mm. Two main fractures, that is, crack 2 and crack 3, are shown in the image. Crack 2 and crack 3 coalesce. Only one main fracture is observed in these images from $z = 5$ to 20 mm, and the fracture system is very simple.

The slice image in Fig. 11b at $y = 50$ mm reveals the top surface crack distribution. Only one main fracture, that is, crack 1, and minor fractures are observed in this image across the diameter direction. At $y = 40$ mm, crack 1 still crosses the diameter direction and crack 2 propagates. However, crack 1 is located near the right boundary of the specimen when y equals 30 mm, indicating that the propagation height along the vertical direction is $\sim$20 mm. The height of $\sim$20 mm corresponds to that shown in Fig. 10a. For crack 2, it only appears in the range of $y = 50$–10 mm, which means that crack 2 is located in the upper part of the specimen. At $y = 10$ mm, crack 3 is initiated in the slice image. With decreasing height from $y = -10$ mm to $y = -30$ mm, crack 3 gradually moves to the center of the specimen, whereas crack 3 distributes discretely along the left boundary of the specimen at $y = -40$ mm.

Furthermore, some minor fractures can be found besides the main fracture in the slice images. Main fractures all are inclined in the specimens and are macro-shear cracks, which implies that the intact numerical specimen failed dominantly due to the development of a steeply inclined macro-crack under triaxial compression.

Figure 12 shows the front vertical and horizontal cross sections of numerical specimen containing two unparallel fissures after triaxial compression failure under a confining pressure of 5 MPa. An upward fracture and a downward fracture can be observed in Fig. 12a at $z = -25$ mm at the left and right tips of the horizontal fissure, respectively. However, no notable fractures are observed near the inclined fissure. This crack distribution agrees well with that of the experimental physical failed specimen (Fig. 12a). Only minor fractures were seen at the lower tip of the inclined fissure at $z = -20$ and 5 mm. However, crack 1 and crack 2 at the tips of the horizontal fissure appear in all front vertical cross sections with different depths. Moreover, they all propagate to the boundary of the specimen. It should be noted that no crack coalescence occurs between the two preexisting fissures.

There is no obvious fracture in the two slice images in Fig. 12b at $y = 50$ mm and -40 mm, which indicates that fractures do not evolve to the two ends of the specimen. When the height decreases from $y = 40$ mm to

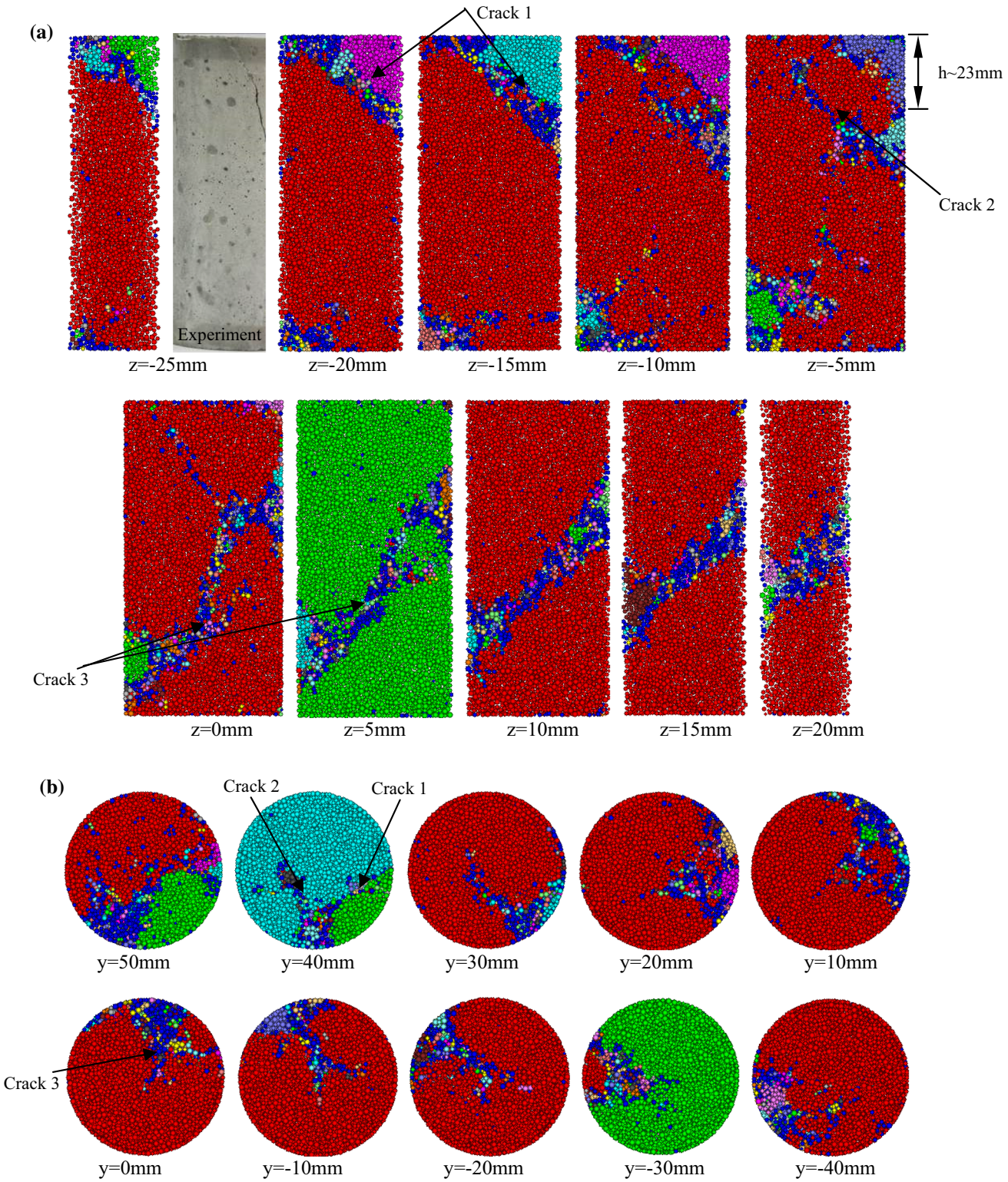

Fig. 11 Cross-section results of intact numerical specimen after triaxial compression failure ($\sigma_3 = 5$ MPa). **a** Front vertical cross sections with different depths; and **b** horizontal cross sections with different heights

$y = 10$ mm, crack 1 propagates from the boundary toward the center of the specimen. Crack 1 and 2 can be observed simultaneously in the horizontal cross section at $y = 10$ mm. With the decrease in height from $y = 10$ mm to $y = 30$ mm, crack 2 grows from the center toward the boundary of the specimen.

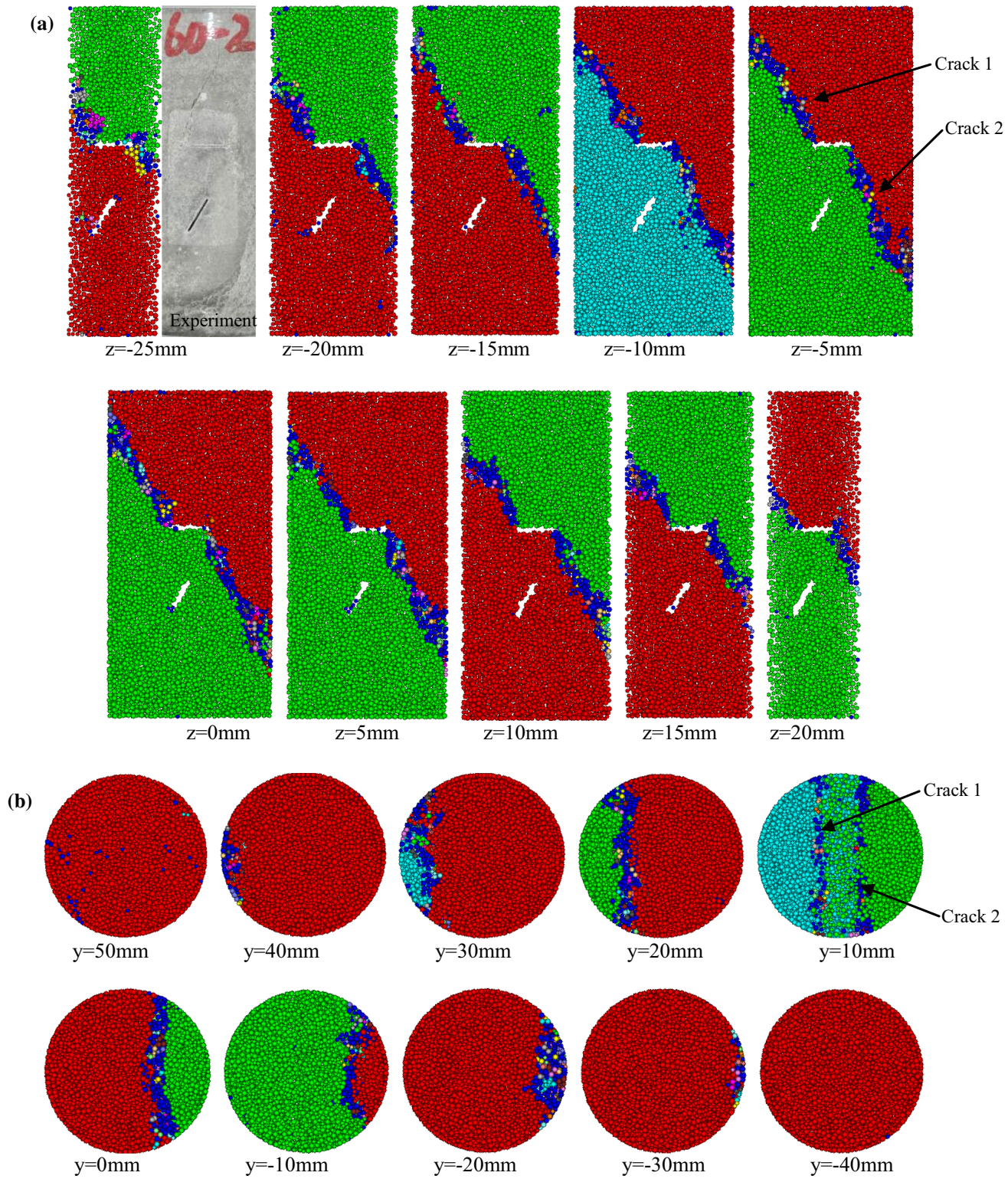

Fig. 12 Cross sections of pre-fissured numerical specimen after triaxial compression failure ($\alpha = 60°$, $\sigma_3 = 5$ MPa). **a** Front vertical cross sections with different depths; **b** horizontal cross sections with different heights

Figure 13 displays the front vertical and horizontal cross sections of the numerical specimen containing two unparallel fissures after triaxial compression failure under a confining pressure of 15 MPa. The images demonstrate a similar crack distribution for the front vertical cross sections with different depths (Fig. 13f), implying that the cracks propagate across

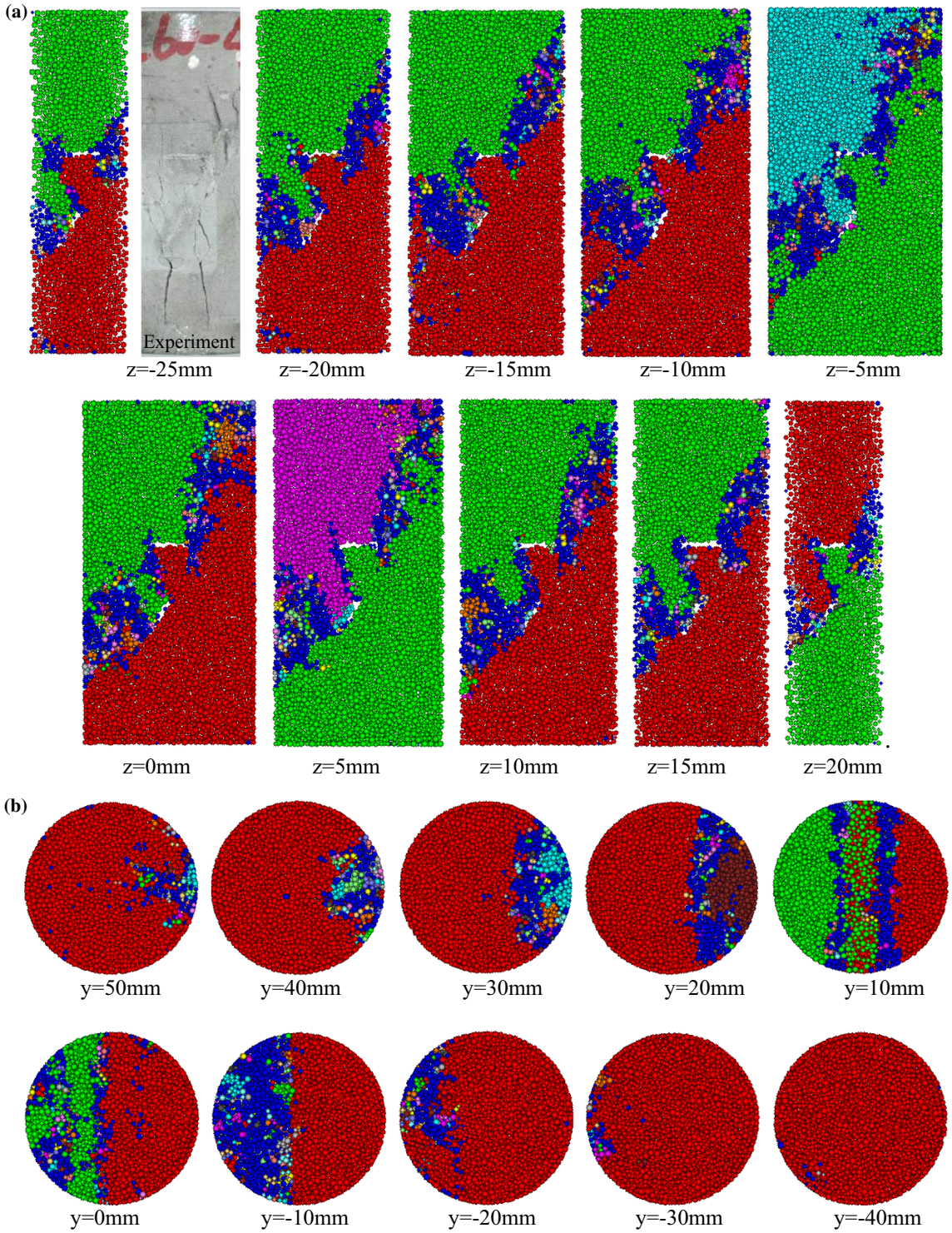

Fig. 13 Cross sections of pre-fissured numerical specimen after triaxial compression failure ($\alpha = 60°$, $\sigma_3 = 15$ MPa). **a** Front vertical cross sections with different depths; and **b** horizontal cross sections with different heights

the whole specimen in the diameter direction (z axial). Fractures of the horizontal cross sections with different heights mainly occur in the range of $y = 50$ to -30 mm. No large cracks can be observed near the bottom of the specimen at $y = -40$ mm, which is similar to the pre-fissured specimen under a confining pressure of 5 MPa (Fig. 12).

Comparing the cross sections of numerical specimen under triaxial compression, some interesting phenomena can be observed.

1. From the comparison between cross sections of intact specimen and pre-fissured specimen under same confining pressure shown in Figs. 11 and 12, we can see that the cracks in the intact specimen under a confining pressure of 5 MPa (Fig. 11) are initiated first at one of the two ends of the specimen and then propagate toward the other end of the specimen (Yang et al. 2015a). However, the cracks in the pre-fissured numerical specimen under a confining pressure of 5 MPa (Fig. 13) first emerge at the tips of preexisting fissures and then grow toward the boundary and surface of the specimen.
2. From the comparison between cross section of pre-fissured specimen under a confining pressure of 5 MPa and 15 MPa shown in Figs. 12 and 13, it is clear that the confining pressure has a significant effect on the internal damage behavior. No crack coalescence was observed between the two pre-fissures under low confining pressure (5 MPa). However, two crack coalescences occur due to propagation tensile wing cracks and anti-wing crack under a medium confining pressure (15 MPa). In addition, anti-wing cracks are closely related to the confining pressure. Taking the anti-wing crack from the lower tip of the inclined fissure as an example, when the confining pressure is low (5 MPa), no anti-wing crack is initiated at the tip, whereas when the confining pressure increases to 15 MPa, an anti-wing crack emanates and forms a link with the right tip of the horizontal fissure.

5 Conclusions

This study investigates the strength failure and internal damage behavior of rock-like material specimens with two unparallel fissures using laboratory experiments and a three-dimensional discrete element method. The following conclusions are drawn from the analysis of experimental and numerical results.

1. A set of micro-mechanical parameters in PFC3D was calibrated from the experimental results of intact rock-like material specimens. The numerical results, including the axial stress–strain curves, peak strength and peak strain, and ultimate failure modes of specimen containing two unparallel fissures under uniaxial and triaxial compression using the calibrated micro-mechanical parameters agree well with the laboratory compression tests. This agreement implies that the calibrated micro-mechanical parameters and setup numerical model have the capability of reproducing laboratory results.
2. The crack initiation, propagation and coalescence process of numerical specimens containing two unparallel fissures are all obtained using PFC3D. Until now, it has been impossible to capture these characteristics with triaxial compressive experiments. The crack evolution process and failure mode of rock-like material specimen containing two unparallel fissures are found to be dependent on fissure angle and confining pressure. When the confining pressure is small, the failure mode is mainly affected by the fissure angle. However, the failure mode is mainly influenced by the confining pressure at a high confining pressure.
3. The crack pattern at different positions was analyzed in detail to explore the internal damage behavior of rock-like material specimen under conventional triaxial compression. The cracks in the intact specimen form first at one end of the specimen and then propagate toward the other end, while the cracks in the pre-fissured numerical specimen emerge first at the tips of preexisting fissures and then grow toward the boundary and surface of the specimen. Anti-wing cracks are closely related to the confining pressure. When the confining pressure is high, anti-wing cracks emanate and propagate strongly.

Acknowledgments The research was supported by the Natural Science Foundation of Jiangsu Province for Distinguished Young Scholars (BK20150005) and the Fundamental Research Funds for the Central Universities (2014YC10). We would also like to acknowledge the editor Giovanni Barla and the anonymous reviewers for their valuable comments, which have greatly improved this paper.

References

Bahaaddini M, Hebblewhite BK, Sharrock G (2013) Numerical investigation of the effect of joint geometrical parameters on the mechanical properties of a non-persistent jointed rock mass under uniaxial compression. Comput Geotech 49(4):206–225

Bobet A (2000) The initiation of secondary cracks in compression. Eng Fract Mech 66(2):187–219

Cao RH, Cao P, Lin H, Pu CZ, Ou K (2016) Mechanical behavior of brittle rock-like specimens with pre-existing fissures under uniaxial loading: experimental studies and particle mechanics approach. Rock Mech Rock Eng 49(3):763–783

Cho N, Martin CD, Sego DC (2007) A clumped particle model for rock. Int J Rock Mech Min Sci 44(7):997–1010

Ding XB, Zhang LY, Zhu HH, Zhang Q (2014) Effect of model scale and particle size distribution on PFC3D simulation results. Rock Mech Rock Eng 47(6):2139–2156

Dyskin AV, Jewell RJ, Joer H, Sahouryeh E, Ustinov KB (1994) Experiments on 3-d crack growth in uniaxial compression. Int J Fract 65(4):77–83

Dyskin AV, Germanovich LN, Ustinov KB (1999) A 3-D model of wing crack growth and interaction. Eng Fract Mech 63(1):81–110

Dyskin AV, Sahouryeh E, Jewell RJ, Joer H, Ustinov KB (2003) Influence of shape and locations of initial 3-D cracks on their growth in uniaxial compression. Eng Fract Mech 70(15):2115–2136

Fan X, Kulatilake PHSW, Chen X (2015) Mechanical behavior of rock-like jointed blocks with multi-non-persistent joints under uniaxial loading: a particle mechanics approach. Eng Geol 190:17–32

Fujii Y, Ishijima Y (2004) Consideration of fracture growth from an inclined slit and inclined initial fracture at the surface of rock and mortar in compression. Int J Rock Mech Min Sci 41(6):1035–1041

Goodman RE (1989) Introduction to rock mechanics. Wiley, New York

Haeri H, Shahriar K, Marji MF, Moarefvand P (2014) Experimental and numerical study of crack propagation and coalescence in pre-cracked rock-like disks. Int J Rock Mech Min Sci 67(4):20–28

Huang D, Gu DM, Yang C, Huang RQ, Fu GY (2016a) Investigation on mechanical behaviors of sandstone with two preexisting flaws under triaxial compression. Rock Mech Rock Eng 49(2):375–399

Huang YH, Yang SQ, Ju Y, Zhou XP, Gao F (2016b) Experimental study on mechanical behavior of rock-like materials containing pre-existing intermittent fissures under triaxial compression. Chin J Geotech Eng 38(7):1212–1220 **(in Chinese)**

Huang YH, Yang SQ, Tian WL, Zeng W, Yu LY (2016c) An experimental study on fracture mechanical behavior of rock-like materials containing two unparallel fissures under uniaxial compression. Acta Mech Sin 32(3):442–455

Huang ZM, Ma ZG, Lei Z, Peng G, Zhang YK, Liu F (2016d) A numerical study of macro-mesoscopic mechanical properties of gangue backfill under biaxial compression. Int J Min Sci Technol 26(2):309–317

Itasca Consulting Group Inc (2008) PFC3D manual, version 4.0. Minneapolis, Minnesota

Lee H, Jeon S (2011) An experimental and numerical study of fracture coalescence in pre-cracked specimens under uniaxial compression. Int J Solids Struct 48(6):979–999

Liang ZZ, Xing H, Wang SY, Williams DJ, Tang CA (2012) A three-dimensional numerical investigation of the fracture of rock specimens containing a pre-existing surface flaw. Comput Geotech 45(9):19–33

Liu LQ, Liu PX, Wong HC, Ma SP, Guo YS (2008) Experimental investigation of three-dimensional propagation process from surface fault. Sci China 51(10):1426–1435

Liu J, Zhu Z, Wang B (2014) The fracture characteristic of three collinear cracks under true triaxial compression. Sci World J. doi:10.1155/2014/459025

Lu Y, Wang L, Elsworth D (2015) Uniaxial strength and failure in sandstone containing a pre-existing 3-D surface flaw. Int J Fract 194(1):59–79

Manouchehrian A, Sharifzadeh M, Marji MF, Gholamnejad J (2014) A bonded particle model for analysis of the flaw orientation effect on crack propagation mechanism in brittle materials under compression. Arch Civil Mech Eng 14(1):40–52

Morgan SP, Johnson CA, Einstein HH (2013) Cracking processes in barre granite: fracture process zones and crack coalescence. Int J Fract 180(2):177–204

Palmstrom A (1995) RMI–a rock mass characterization system for rock engineering purposes. Oslo University, Norway

Sahouryeh E, Dyskin AV, Germanovich LN (2002) Crack growth under biaxial compression. Eng Fract Mech 69(18):2187–2198

Turichshev A, Hadjigeorgiou J (2015) Experimental and numerical investigations into the strength of intact veined rock. Rock Mech Rock Eng 48(5):1897–1912

Wang SY, Sloan SW, Sheng DC, Yang SQ, Tang CA (2014) Numerical study of failure behaviour of pre-cracked rock specimens under conventional triaxial compression. Int J Solids Struct 51(5):1132–1148

Wong RHC, Chau KT (1998) Crack coalescence in a rock-like material containing two cracks. Int J Rock Mech Min Sci 35(2):147–164

Wong RHC, Law CM, Chau KT, Zhu WS (2004) Crack propagation from 3-D surface fractures in pmma and marble specimens under uniaxial compression. Int J Rock Mech Min Sci 41(3):37–42

Yang SQ, Jiang YZ, Xu WY, Chen XQ (2008) Experimental investigation on strength and failure behavior of pre-cracked marble under conventional triaxial compression. Int J Solids Struct 45(17):4796–4819

Yang L, Jiang Y, Li S, Li B (2014a) Experimental and numerical research on 3D crack growth in rocklike material subjected to uniaxial tension. J Geotech Geoenviron Eng 139(10):1781–1788

Yang SQ, Huang YH, Jing HW, Liu XR (2014b) Discrete element modeling on fracture coalescence behavior of red sandstone containing two unparallel fissures under uniaxial compression. Eng Geol 178(16):28–48

Yang SQ, Ranjith PG, Gui YL (2015a) Experimental study of mechanical behavior and X-ray micro CT observations of sandstone under conventional triaxial compression. Geotech Test J 38(2):179–197

Yang XX, Kulatilake PHSW, Jing HW, Yang SQ (2015b) Numerical simulation of a jointed rock block mechanical behavior adjacent to an underground excavation and comparison with physical model test results. Tunn Undergr Space Technol 50:129–142

Yin P, Wong RHC, Chau KT (2014) Coalescence of two parallel pre-existing surface cracks in granite. Int J Rock Mech Min Sci 68(6):66–84

Zhang Q, Zhu H, Zhang L, Ding X (2011) Study of scale effect on intact rock strength using particle flow modeling. Int J Rock Mech Min Sci 48(8):1320–1328

Zhou Y, Wu SC, Gao YT, Misra A (2014) Macro and meso analysis of jointed rock mass triaxial compression test by using equivalent rock mass(ERM) technique. J Cent South Univ 21(3):1125–1135

Zhu TT, Jing HW, Su HJ, Yin Q, Du MR, Han GS (2016) Physical and mechanical properties of sandstone containing a single fissure after exposure to high temperatures. Int J Min Sci Technol 26:319–325